International Journal of Nanomedicine

Dovepress
Taylor & Francis Group

Open Access Full Text Article

ORIGINAL RESEARCH

GLX351322-Loaded Nanoparticles Alleviate Chronic Stress-Induced Depressive Behaviors Through Inhibition of Ferroptosis and Oxidative Stress

Tian Wang[1], Junyan An[2], Xiying Fu[3], Jiangjin Sun[1], Haiping Li[1,4], Xiaoou Han[1], Wei Yang[1]

[1]Department of Neurology, The Second Hospital of Jilin University, Changchun, Jilin Province, People's Republic of China; [2]Department of Neurosurgery, China-Japan Union Hospital of Jilin University, Changchun, Jilin Province, People's Republic of China; [3]Department of Endocrinology, The Second Hospital of Jilin University, Changchun, Jilin Province, People's Republic of China; [4]Department of Neurology, The Affiliated Hospital of Bei-Hua University, Jilin, Jilin Province, People's Republic of China

Correspondence: Wei Yang, Email wyang2002@jlu.edu.cn

Purpose: Depression is a widespread neuropsychiatric disorder with limited treatment efficacy and frequent adverse effects. Ferroptosis, an iron-dependent and oxidative stress (OS) - related form of regulated cell death, is emerging as a key pathogenic mechanism in neurological diseases, yet its role in depression remains largely unexplored. This study aimed to evaluate the antidepressant and neuroprotective potential of GLX351322 (GLX), a selective inhibitor of NADPH oxidase 4 (NOX4), by formulating it into a nanocarrier system to overcome its pharmacokinetic limitations.

Methods: GLX was encapsulated into methoxy poly (ethylene glycol)-poly(ε-caprolactone) (mPEG-PCL) nanoparticles (GLX-NPs) via a simple nanoprecipitation method. Including particle size, zeta (ζ) potential, morphology, drug loading (DL), encapsulation efficiency (EE), biodistribution, and release efficiency, were characterized. In vivo, the antidepressant effect was assessed using a chronic unpredictable mild stress (CUMS) mouse model, while in vitro, the safety profile was evaluated in CORT-induced HT22 cells. Fluorescence, Quantitative real-time PCR (qRT-PCR), and Western blot (WB) experiments were conducted to explore the underlying neuroprotective mechanisms.

Results: The average particle size of GLX-NPs was 43.58 ± 3.09 nm, with a ζ potential of approximately −12.13 ± 0.35 mV, a DL of 6.90%, and an EE of 88.79%. GLX-NPs increased the accumulation of the drug in brain tissues. In CUMS mice, GLX-NPs improved depressive-like behaviors and preserved hippocampal neuronal integrity. Mechanistically, GLX-NPs inhibited NOX4 expression, suppressed reactive oxygen species (ROS) production and lipid peroxidation, and activated the Nrf2/HO-1/GPX4 pathway to alleviate ferroptosis. Co-administration with ferroptosis inducers or Nrf2 inhibitors reversed these protective effects.

Conclusion: GLX-NPs effectively alleviate depressive-like behaviors by inhibiting neuronal ferroptosis and OS via modulation of the NOX4/Nrf2/HO-1/GPX4 signaling pathway. This study supports the therapeutic potential of GLX-NPs as a novel nanomedicine targeting ferroptosis in the treatment of depression.

Keywords: Depression, nanoparticle, oxidative stress, ferroptosis, NOX4

Introduction

Depression is a widespread neuropsychiatric disorder that severely impacts an individual's physical health and daily life, imposing a substantial burden on individuals and society.[1] Despite the availability of numerous classes of antidepressant medications, a significant proportion of patients exhibit suboptimal therapeutic responses,[2,3] often accompanied by severe adverse effects such as weight fluctuations, insomnia, and suicidal ideation.[4–7] Thus, there remains an urgent need to develop safer and more effective treatment strategies.

Received: 21 July 2025
Accepted: 13 November 2025
Published: 24 November 2025

Graphical Abstract

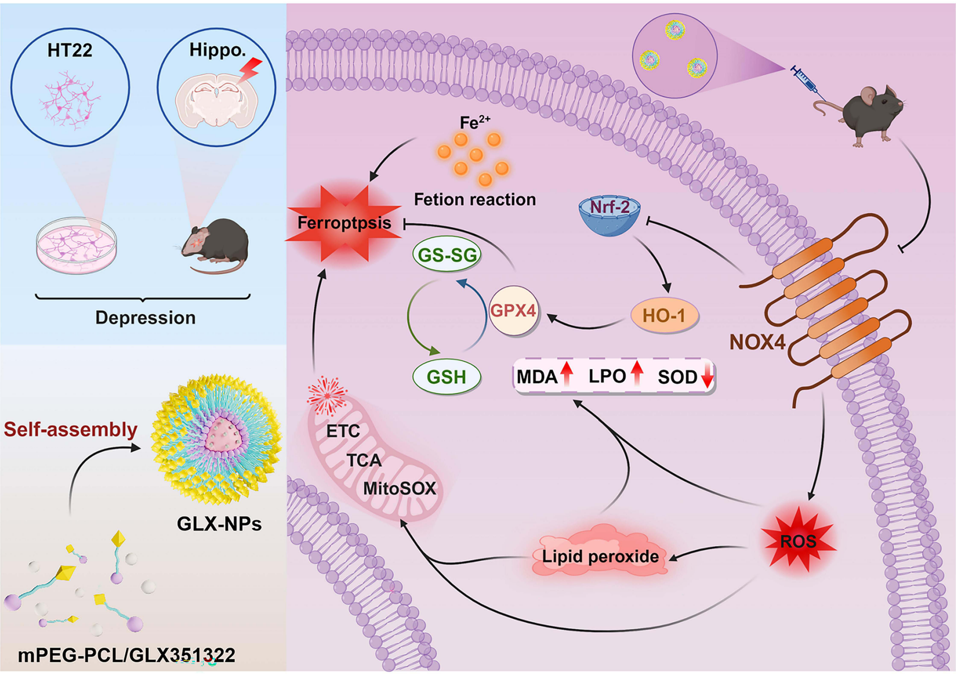

The blood-brain barrier (BBB) is one of the main obstacles to drug delivery to the brain, and overcoming this barrier to enable efficient drug penetration remains a significant challenge in drug development. In recent years, nanomedicine has gained widespread attention as an innovative therapeutic strategy due to its ability to significantly enhance the bioavailability and stability of drugs. In particular, polymeric nanomicelles (PNMs) have become a research focus in drug delivery systems because of their excellent drug loading capacity, good biocompatibility, and biodegradability.[8,9] PNMs can form colloidal systems with a core-shell structure through the self-assembly properties of amphiphilic copolymers.[10] Methoxy polye (thylene glycol)-poly(ε-caprolactone) (mPEG-PCL) is a typical amphiphilic copolymer that spontaneously forms micelles in water, with a hydrophilic PEG shell and a hydrophobic PCL core, which effectively encapsulates hydrophobic drugs in its hydrophobic core, significantly improving drug solubility and controlling drug release.[11] Moreover, mPEG-PCL nanomicelles have a small particle size, typically in the range of 50–200 nm,[10] allowing them to more easily penetrate the BBB and enter the brain tissue.[12] These outstanding properties make mPEG-PCL a key material in drug delivery, particularly showing great potential for central nervous system (CNS) therapy.

GLX351322 (GLX) is a small molecule NADPH oxidase 4 (NOX4) inhibitor that has demonstrated significant neuroprotective effects in neurodegenerative disease models, such as Alzheimer's disease (AD) and Parkinson's disease (PD).[13–15] Nevertheless, the potential application of GLX in the treatment of depression has not been systematically studied. Especially due to its poor solubility and low bioavailability, the therapeutic potential of GLX is limited. To overcome these limitations, we encapsulated GLX into mPEG-PCL using a simple nanoprecipitation method to form polymeric nanoparticles (GLX-NPs), thereby enhancing its drug delivery efficiency.

NOX4, as a key enzyme in reactive oxygen species (ROS) generation, is widely involved in oxidative stress (OS) responses in neurological disorders.[16–18] In the complex biological mechanisms of depression, OS is considered an important pathological basis. According to the "OS hypothesis of depression", excessive ROS production and impaired antioxidant defense systems lead to structural and functional damage in the brain.[19] Therefore, inhibiting the overexpression of NOX4 appears to be a potential therapeutic approach for depression. Additionally, the excessive accumulation of ROS not only exacerbates oxidative damage in cells but also triggers ferroptosis. Ferroptosis is an iron-dependent, non-apoptotic form of cell death regulated by OS, which has been identified as a key pathogenic mechanism in various neurodegenerative diseases.[20–22] However, its role in depression remains unclear. A substantial body of evidence suggests a vicious cycle between excessive ROS generation and ferroptosis. On one hand, the accumulation of excessive ROS exacerbates oxidative damage in cells, promoting the release and accumulation of iron, thereby accelerating ferroptosis. On the other hand, ferrous ions (Fe^{2+}) in cells catalyze ROS generation through the Fenton reaction, further driving lipid peroxidation,[23] which amplifies neuronal dysfunction and degeneration. Therefore, as a NOX4 inhibitor, GLX-NPs demonstrate therapeutic potential in reducing OS and inhibiting ferroptosis.

The Nrf2/HO-1/GPX4 pathway is considered a key regulator of OS and ferroptosis.[24,25] This pathway has been shown to be activated under conditions that inhibit NOX4 in various neurological disorders, such as memory impairments induced by sleep deprivation[26] and Alzheimer's disease,[27] exerting protective effects against ferroptosis and neurodegeneration. However, whether this pathway alleviates depressive-like behaviors remains unclear. In light of this, we encapsulated GLX in mPEG-PCL and characterized the resulting nanoparticles. We hypothesize that GLX-NPs might regulate NOX4, thereby influencing the expression of Nrf2/HO-1/GPX4, inhibiting neuronal ferroptosis, and ultimately improving depressive symptoms. To test this hypothesis, we established chronic unpredictable mild stress (CUMS) mouse models and CORT-induced HT22 cell models. Our results demonstrate that GLX-NPs effectively ameliorate depressive behaviors, inhibit ferroptosis in hippocampal neurons, reduce hippocampal neuronal damage, restore redox balance, and protect mitochondrial integrity. These findings highlight the potential of GLX-NPs as a promising therapeutic strategy in the treatment of depression. Moreover, the neuroprotective effects observed suggest that the Nrf2/HO-1/GPX4 pathway plays a crucial role in mediating these benefits, thus offering a novel perspective for developing targeted interventions in depression therapy.

Materials and Methods

Preparation of GLX-Loaded mPEG-PCL Micelles

We referred to previous studies[11,28] and explored the optimal ratio between GLX and mPEG-PCL for the preparation of GLX-loaded micelles (Table S1). Specifically, 0.7 mg of GLX (HY-100111, MCE, USA) and 9.3 mg of mPEG5k-PCL5k (JP0051, Jingpi Technology, China) were fully dissolved in 3 mL of N, N-dimethylformamide (DMF, B010697-1L, Energy Chemical, China) as the organic phase. The mixture was stirred thoroughly at 400 rpm for 30 minutes to ensure complete dissolution. Afterward, it was added dropwise into 5 mL of distilled water under magnetic stirring at 2500 rpm to ensure uniform dispersion. Subsequently, the solution was subjected to ultrasonic treatment for 10 minutes using an ultrasonic bath at a frequency of 40 kHz at room temperature to eliminate air bubbles and enhance micelle formation. The solution was then dialyzed against Milli-Q water (MWCO 3500 Da) for 8 hours, with the water being replaced every hour to ensure the complete removal of DMF. The final product, GLX-NPs, was obtained. After dialysis, the solution was centrifuged at 15,000 rpm for 10 minutes and filtered through a 0.22 μm membrane to remove any unencapsulated drug (Figure 1A).

Characterization of GLX-Loaded mPEG-PCL Micelles

Assessment of Size Distribution and Electrokinetic Properties

The particle size and zeta (ζ) potential of GLX-NPs micelles were detected through dynamic light scattering (DLS) using a Zetasizer Nano ZS analyzer (Zetasizer Ultra, Malvern Instruments, UK). All measurements were performed at a controlled temperature of 25 °C.

Morphology

The structural characteristics of the micelles were visualized by transmission electron microscope (TEM, HT7800, Hitachi, Japan). Both unloaded mPEG-PCL (NPs, without GLX) and GLX-NPs micelles were separately dispersed in Milli-Q water and deposited onto a carbon-coated copper grid. Negative staining was performed using phosphotungstic acid, followed by air-drying under ambient conditions.

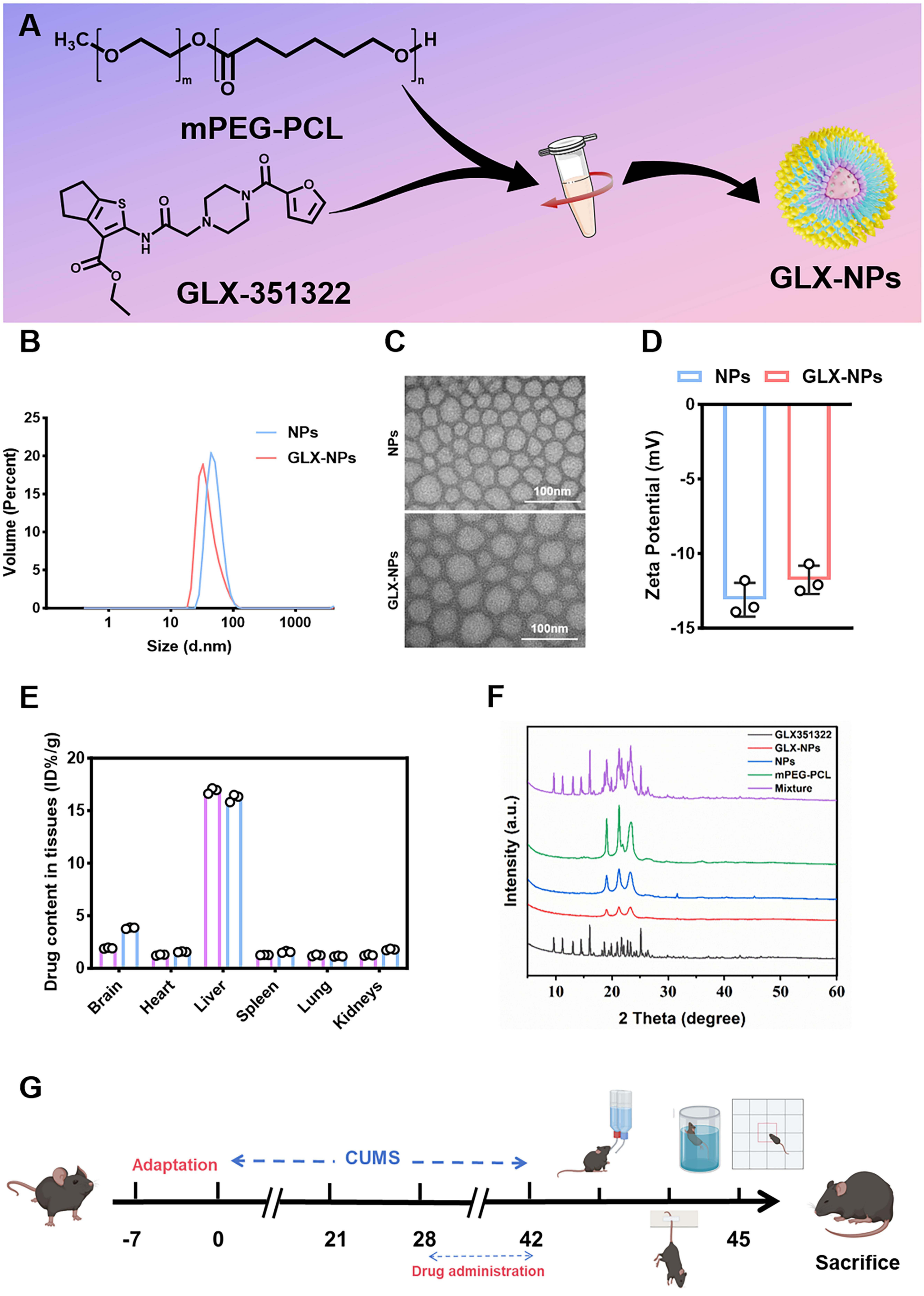

Figure 1 Synthesis and characterization of GLX-NPs. (**A**) Schematic illustration of the preparation process of GLX-NPs. (**B**) Particle size distribution of GLX-NPs and NPs. (**C**) TEM image of GLX-NPs and NPs. (**D**) Zeta potential of GLX-NPs and NPs (n=3). (**E**) Biodistribution of GLX and GLX-NPs in various tissues at 24 hours post-administration (n = 3). (**F**) XRD patterns of the GLX-NPs and other formulations. (**G**) Timeline of the animal experiments.

Drug Loading (DL), Encapsulation Efficiency (EE), Biodistribution, and in vitro Release Kinetics

High-performance liquid chromatography (HPLC, Elite 3100, E-Classical, China) was employed in conjunction with a reversed-phase C18 column (Supersil ODS2, 5 μm, E-Classical, China) to quantify DL, EE, and the distribution of GLX and its nanoformulation in various organs, including the brain, heart, liver, spleen, lungs, and kidneys. The column temperature was maintained at 30°C, and the flow rate was set to 1 mL/min. The mobile phase consisted of methanol and water (containing 0.05% TFA), and HPLC separation was performed at 254 nm with a gradient from 20/80 to 80/20 (v/v). DL and EE were calculated according to the following formulas:

$$\mathrm{DL}\ (\%) = \frac{\mathrm{M}_{\text{Amount of drug in GLX}-\text{NPs}}}{\mathrm{M}_{\text{Total amount ofGLX}-\text{NPs}}} \times 100\%$$

$$\mathrm{EE}\ (\%) = \frac{\mathrm{M}_{\text{Amount of drug inmicelles}}}{\mathrm{M}_{\text{Total amount of drug added}}} \times 100\%$$

GLX or GLX-NPs were administered to CUMS model mice, followed by euthanasia at 6, 12, and 24 hours post-dosing to collect tissue specimens from the brain, heart, liver, spleen, lungs, and kidneys. The harvested tissues were homogenized and subjected to methanol extraction. The resulting supernatants were passed through 0.22 μm membrane filters and analyzed using HPLC.

Additionally, the in vitro release kinetics of GLX-NPs were evaluated using the same HPLC method. Briefly, 1 mL of GLX-NPs solution was placed in a dialysis bag (molecular weight cutoff: 3.5 kDa). The dialysis bag was then immersed in 30 mL of phosphate-buffered saline (PBS, pH 7.4) containing 0.5% (w/w) Tween 80 (HY-Y1891, MCE, USA) and incubated at 37°C under gentle shaking. At predetermined time intervals, the amount of drug released into the incubation medium was quantitatively determined.

Crystallographic Analysis by Powder X-Ray Diffraction (XRD)

The crystallographic analysis of pure drug, physical mixtures, polymer, blank nanoparticles, and drug-loaded nanoparticles was performed using a powder X-ray diffraction (XRD) instrument (D8-ADVANCE, Bruker, Germany) equipped with a Cu Kα radiation source at 40 kV and 20 mA. Before analysis, each sample was compressed into thin films using a tablet press and placed on a steel holder. XRD data were collected in the 2θ range of 5° to 60° with a scanning rate of 7°/min.

Animals

C57BL/6J mice (Male, 18–20 g) were sourced from Jilin University. Animals were housed under standardized laboratory conditions. All experimental protocols were approved by the Animal Ethics Committee of Jilin University and conducted in accordance with internationally accepted guidelines for the ethical use of laboratory animals (No. SY. 2024–10-005).

CUMS-Based Depression Induction Protocol

CUMS regimen was implemented with slight modifications to previously described protocols.[29,30] Following a seven-day acclimatization phase, animals were exposed to a series of stressors intended to produce sustained and unpredictable psychological pressure. The regimen consisted of stressors such as: 24-hour fasting, 5-minute forced swims at 4 °C and 45 °C respectively, 2-hour restraint, 1-minute tail pinch, 6-hour cage tilting at a 45° angle, 24-hour exposure to damp bedding, 24-hour water deprivation, 24 hours in an empty cage, and 5-minute cage shaking. To maintain unpredictability, a different stressor was randomly applied each day over a continuous six-week period.

Group and Drug Treatment

Experiment 1: A total of 36 mice were randomly divided into 6 experimental groups (n=6 per group): Control, CUMS, CUMS+ NPs, CUMS+GLX (5.0 mg/kg, HY-100111, MCE, USA), CUMS+GLX-NPs (5.0 mg/kg), CUMS+ fluoxetine (Flu, 20.0 mg/kg, PHR1394, Sigma-Aldrich, USA). All animals were exposed to chronic CUMS for a period of six

https://doi.org/10.2147/IJN.S555165

weeks except for the control group. Drug treatments were initiated at the beginning of week 5 and continued daily for the final two weeks while CUMS exposure persisted. GLX and Flu were administered via intraperitoneal injection (i.p). GLX-NPs were administered intravenously (i.v). via the tail vein. A blank nanoparticle group (CUMS + NPs, i.v). was included to control for the effect of the nanocarrier. The therapeutic doses of GLX-NPs and Flu were determined based on preliminary experiments (Figure S1A–H) and previous studies.[31]

Experiment 2: This experiment consisted of five groups of mice (n = 6 per group): Control, CUMS, CUMS + GLX-NPs (5 mg/kg), CUMS + GLX-NPs + RSL3 (5.0 mg/kg, HY-100218A, MCE, USA), and CUMS + Ferrostatin-1 (Fer-1, 5.0 mg/kg, HY-100579, MCE, USA). The drug administration schedule was the same as in Experiment 1. Fer-1 and RSL3 were administered via i.p. In the combination group (GLX-NPs + RSL3), RSL3 was followed by intravenous administration of GLX-NPs 1 hour after RSL3 administration, in order to minimize potential pharmacokinetic interactions. The administration approach and dosage of RSL3 and Fer-1 were based on protocols reported in earlier studies.[32,33]

Experiment 3: This experiment consisted of four groups of mice (n = 6 per group): control, CUMS, CUMS + GLX-NPs (5.0 mg/kg), and CUMS + GLX-NPs + ML385 (30.0 mg/kg, HY-100523, MCE, USA). The drug administration schedule was the same as in Experiment 1. In the combination group, ML385 was administered first via intraperitoneal injection, followed by intravenous GLX-NPs after a 1-hour interval. The ML385 dosage was determined according to findings from prior research.[34]

Behavioral Testing

Sucrose Preference Test (SPT)

To reduce novelty-induced stress, mice were individually housed during the habituation period and provided with two bottles of 1% (w/v) sucrose solution for 24 hours. Subsequently, they were exposed to one bottle containing 1% sucrose solution and another with distilled water for an additional 24 hours. To avoid spatial bias, bottle placement was alternated every 2 hours. Prior to the formal assessment, mice underwent a 12-hour deprivation of both food and water. Following the deprivation, each mouse received two pre-weighed bottles—one containing 1% sucrose and the other distilled water—and was permitted to drink freely for a duration of 4 hours. The remaining volume in each bottle was measured post-test to determine intake. To quantify sucrose preference, the following equation was applied: Sucrose Preference (%) = sucrose consumption / (sucrose consumption + distilled water consumption) × 100%.

Tail Suspension Test (TST)

Medical tape was attached 1–2 cm from the tail tip to suspend mice individually during the test. The device maintained the mice in an unobstructed head-down orientation by suspending them 50 cm above ground level. The total test duration was 6 minutes, with the initial 2 minutes considered as an acclimatization phase. Immobility time was quantified during the remaining 4 minutes. A state of immobility was identified when no active movement of the limbs or body was observed, excluding motions attributed to breathing. Behavioral responses were documented via video recordings for post hoc analysis.

Forced Swim Test (FST)

For the forced swim test, individual mice were placed in cylindrical glass containers (35 cm × 15 cm) filled with fresh water (12–15 cm depth; temperature: 25–27 °C). At the time of behavioral assessment, each mouse was placed individually in the water-filled cylinder for 6 minutes while behavior was recorded. The first 2 minutes were considered adaptation and not analyzed. Immobility time during the last 4 minutes, defined as minimal movement to keep the head above water, was recorded. Each mouse was tested once. After each test, the water was changed and the cylinder cleaned. Mice were dried and returned to their cages to recover.

Open Field Test (OFT)

Each mouse was individually introduced into a square open-field chamber (dimensions: 50 × 50 × 40 cm) and allowed to explore freely for 5 minutes. The spontaneous locomotor behavior was captured via video recording and subsequently analyzed using the EthoVision XT13 system (Noldus Information Technology, Netherlands). To prevent olfactory interference between trials, the apparatus was thoroughly sanitized with 75% ethanol after each session.

Hematoxylin-Eosin (HE) and Nissl Staining

Mice were anesthetized using 3% isoflurane (R510-22-10, Reward Life Science, China), followed by transcardial perfusion with physiological saline and subsequent fixation using 4% paraformaldehyde (BL539A, Biosharp, China). After dissection, brain specimens were incubated in 4% paraformaldehyde at 4 °C for at least 12 hours to achieve post-fixation. The specimens underwent dehydration, paraffin embedding, and sectioning. Rehydration was performed after deparaffinization. Final staining and sealing with neutral resin were performed.

To further assess neuronal injury, Nissl staining was performed. Paraffin-embedded brain sections were deparaffinized, rinsed thoroughly, and then stained according to the supplier's guidelines (G1086, Servicebio, China). the slides were briefly washed twice with distilled water, dehydrated through an ethanol series, and sealed using neutral resin. Hippocampal tissue morphology was visualized under the microscope (BX51, Olympus Corporation, Japan).

Immunofluorescence

Frozen brain tissue was equilibrated at room temperature for approximately 5 minutes before employing sodium citrate buffer to promote antigen repair. Primary antibodies were incubated at 4°C overnight. The following day, sections were incubated with fluorescently labeled secondary antibody for 1 h at room temperature under light-avoidance conditions. Nuclear staining was accomplished using DAPI. Fluorescent images were acquired using a microscope (IX73, Olympus, Japan).

For cellular staining, cell crawls were fixed with paraformaldehyde and washed with PBS. Subsequently, the samples were blocked in 10% goat serum containing 0.3% Triton X-100 for at least 1 hour. Primary antibody treatment was performed overnight at 4°C. Upon returning to room temperature the next day, the cells underwent three PBS washes, each lasting 5 minutes. Secondary antibody incubation was then conducted for 1 hour. DAPI was applied for nuclear visualization, and the samples were mounted for analysis. Fluorescent imaging was performed with a microscope (IX73, Olympus, Japan). The list of antibodies used in detail is shown in Table S2.

Assessment of Oxidative Stress and Corticosterone (CORT) Levels

Samples including tissue homogenates, serum, and cell extracts were obtained and prepared for subsequent analysis. CORT (BP02183, Baipeng Bio, China), 5-hydroxytryptamine (5-HT, BP01315, Baipeng Bio, China), Fe^{2+} (BC5415, Solarbio, China), malondialdehyde (MDA, S0131S, Beyotime, China), reduced glutathione (GSH, A006-2-1, Nanjing Jiancheng, China), total superoxide dismutase (SOD, A001-3-2, Nanjing Jiancheng, China), and lipid peroxide (LPO, BC5245, Solarbio, China) was used as specified by the supplier's recommended protocol.

Cell Treatment

In the experiment, HT22 cells incubated with GLX-NPs (20 μM, 2h) or Fer-1 (5 μM, 2h, HY-100579, MCE, USA) were treated with CORT (200 μg/mL, 24h, HY-B1618, MCE, USA). HT22 cells incubated with GLX-NPs (20 μM, 2 h) and RSL-3 (5 μM, 2h, HY-100218A, MCE, USA) were stimulated with CORT (200 μg/mL, 24h). HT22 cells incubated with GLX-NPs (20 μM, 2h) and ML385 (5 μM, 2h) were exposed with CORT (200 μg/mL, 24h).

Assessment of Cytotoxicity

HT22 cells were incubated with a working solution of CCK-8 (C0037, Beyotime, China) for 2 hours. At the end of incubation, absorbance was measured at 450 nm using a microplate reader (Spark, TECAN, Austria). The resulting optical density values were used to assess cell viability.

Western Blot (WB) Analysis

Proteins from brain tissues or cells were extracted using RIPA lysis buffer, and concentrations were determined using the BCA protein quantification kit (P0012, Beyotime, China). Equal amounts of protein were resolved by SDS-PAGE and electrotransferred onto PVDF membranes using a blotting apparatus. Membranes were blocked in 5% non-fat milk solution and incubated overnight at 4 °C with primary antibodies (detailed in Table S3). After washing, membranes were probed with horseradish peroxidase-conjugated secondary antibodies for 1 hour at ambient temperature. Signal detection was performed using enhanced chemiluminescence (ECL, 5200, Tanon, China).

Quantitative Real-Time PCR (qRT-PCR)

RNA from brain tissues and cells was extracted using TRIzol reagent (ET101-01, TransGen Biotech Co., Ltd, China) and complementary DNA (cDNA) was synthesized by reverse transcription. qRT-PCR was carried out using SYBR Green Master Mix (AQ601, TransGen Biotech Co., Ltd, China). The primer sequences for NOX4, Nrf2, HO-1, GPX4, and β-actin are provided in Table S4.

Transmission Electron Microscopic Analysis

The hippocampal tissues or HT22 cells were initially fixed with 2.5% glutaraldehyde for 2 hours, followed by prolonged fixation for 24 hours (4 °C). Post-fixation was performed using 1% osmium tetroxide at room temperature for an additional 2 hours. After fixation, the sections were sequentially dehydrated, embedded, sectioned, and subsequently stained by uranyl acetate and lead citrate. Imaging was conducted using a TEM (JEM-1400, JEOL, Tokyo, Japan).

Mitochondrial Membrane Potential (MMP) Detection

After cell samples were prepared, 1 mL of JC-1 staining solution was added for staining (M8650, Solarbio, China). Excess dye was removed by washing twice with JC-1 buffer. A confocal laser scanning microscope (FV3000, Olympus Corporation, Tokyo, Japan) was employed to acquire and visualize fluorescence.

Intracellular Fe^{2+} Levels Detection

Intracellular Fe^{2+} levels were determined using the FerroOrange fluorescent dye (G1727, Servicebio China). HT22 cells were gently washed twice with serum-free medium after the culture medium was aspirated. Cells were subsequently maintained at 37 °C in darkness for 30 minutes in a 1 µmol/L FerroOrange solution formulated in serum-free medium.

Lipid Peroxidation Detection

HT22 cells were cultured in 6-well plates before being incubated with 2 µM C11-BODIPY (581/591), following the manufacturer's protocol (S0043M, Beyotime, China). Fluorescence signals were captured using a laser scanning confocal microscope (FV3000, Olympus Corporation, Japan). The oxidized form of the probe (O-BODIPY) was excited/emitted at 488/510 nm, while the reduced form (R-BODIPY) was visualized at excitation/emission wavelengths of 581/591 nm.

Intracellular ROS and Mitochondrial ROS Detection

Intracellular ROS were assessed using the fluorescent dye 2′,7′-dichlorodihydrofluorescein diacetate (DCFH-DA, S0033S, Beyotime, China) via fluorescence staining (IX73, Olympus, Japan) combined with flow cytometry (FACS Canto II, BD, USA). Cells were induced and incubated with DCFH-DA for 30 minutes in the absence of light.

To evaluate mitochondrial ROS, cells were seeded in confocal dishes and treated with 5 µM MitoSOX at 37 °C for 20 minutes (M36008, Thermo Fisher Scientific, USA). After staining, they were washed twice with PBS and then incubated with Hoechst 33342 for nuclear labeling for an additional 10 minutes.

Statistical Analysis

All data are reported as mean ± S.D. Statistical evaluation employed one-way ANOVA followed by Tukey's test, with significance set at $p < 0.05$. A minimum of three independent replicates were used for each experiment.

Results

Particle Size and ζ Potential of GLX-NPs

DLS analysis was performed to characterize the hydrodynamic diameter and surface charge of the nanoparticles. The results demonstrated that the average hydrodynamic sizes of NPs and GLX-NPs were 50.03 ± 0.47 nm and 43.58 ± 3.09 nm (Figure 1B), respectively. The relatively smaller size of GLX-NPs may be attributed to enhanced intermolecular interactions upon GLX encapsulation, which could result in a more compact nanoparticle structure. TEM was employed to examine the micellar morphology of both NPs and GLX-NPs, as depicted in Figure 1C. The micelles of both NPs and

GLX-NPs exhibited a spherical shape, with the average diameter of NPs being 46.57 nm and GLX-NPs showing a slightly smaller average diameter of 39.46 nm. The ζ potentials of PEG-PCL and GLX-NPs were measured as −12.73 ± 1.77 mV and −12.13 ± 0.35 mV (Figure 1D), respectively. The negative surface charge, along with PEGylation, contributed to improved colloidal stability by inhibiting particle aggregation and reducing macrophage-mediated clearance, thereby prolonging systemic circulation time.[35] These characteristics are favorable for the efficient delivery of GLX-NPs across the BBB.

DL, EE and Biodistribution, and In Vitro Release Kinetics

In this study, we initially measured the DL and EE of GLX using different ratios of mPEG-PCL to GLX, and based on these measurements, determined the optimal ratio of 9:9.3. At this ratio, the prepared GLX-NPs achieved a drug loading of 6.90% and an encapsulation efficiency of 88.79%. These parameters are crucial for optimizing the therapeutic efficacy and delivery efficiency of nanoparticles. DL directly influences the therapeutic effect and effective dose, while EE reflects the stability and bioavailability of the drug within the delivery system.

Furthermore, we evaluated the organ distribution of GLX and GLX-NPs at different time points in the CUMS model mice. The results showed that GLX-NPs consistently exhibited higher brain drug accumulation at all time points compared to free GLX (Figure 1E for 24 hours, Figure S2A for 6 hours, Figure S2B for 12 hours). Notably, between 12 and 24 hours, the drug concentration in the free GLX group decreased by approximately 44.91%, while the GLX-NPs group showed only a decline of 15.69%. This difference indicates that the drug concentration in the free drug group decreased at a rate 2.8 times faster than that in the GLX-NPs group, further suggesting that the nanoparticle-based formulation significantly prolongs the retention time of the drug in the brain and exhibits superior controlled release properties, thereby enhancing the therapeutic efficacy of the drug.

Additionally, we investigated the release profile of GLX-NPs based on in vitro release experiments. As shown in Figure S2C, GLX-NPs released 10.75% of the drug within the first 8 hours, followed by a slower release phase, reaching 52.22% at 120 hours. From 120 to 168 hours, the release continued, but the increase was smaller, with only about 11.77% more released, further supporting the sustained release characteristics of the nanoparticles over a prolonged period. These results highlight the potential of GLX-NPs for controlled release and prolonged drug delivery.

Crystallographic Behavior and Physical Properties Analysis of Nanoparticles

To elucidate the crystalline form changes of GLX in nanoparticle formulations, we analyzed GLX, GLX-NPs, NPs, mPEG-PCL, and physical mixtures using XRD (Figure 1F).

Firstly, GLX exhibited typical crystalline characteristics, with distinct characteristic peaks observed at 9.6°, 11.1°, 13.07°, and 14.47° in the XRD spectrum. These peaks indicate that GLX exists in a crystalline form, with a well-defined crystalline structure. Crystalline drugs typically dissolve more slowly, and thus, the crystalline form of GLX may influence its solubility and bioavailability, subsequently affecting its release rate and absorption efficiency.

In contrast, the XRD spectrum of GLX-NPs displayed a smooth curve without the characteristic peaks of GLX, suggesting that GLX has transformed into an amorphous state within the nanoparticle carrier system. Amorphous drugs generally exhibit higher solubility and faster absorption rates. This observation further supports that GLX-NPs not only improve the solubility of the drug but also possess good dispersion properties, significantly enhancing the drug's bioavailability.

For the physical mixture samples, the individual components retained their respective crystalline structures, indicating that no intermolecular interactions or changes in the crystalline structure occurred within the formulation. This result suggests that in the physical mixture, the interaction between the drug and the carrier is weak, and no new solid phases or complexes were formed.

GLX-NPs Alleviate Depression-Like Behaviors in Mice Exposed to CUMS

To evaluate the potential antidepressant effects of GLX-NPs on mice subjected to CUMS, a battery of behavioral tests was conducted, including the OFT, FST, TST, and SPT. The experimental timeline is illustrated in Figure 1G, and body weight changes during the modeling and treatment period are shown in Figure 2A.

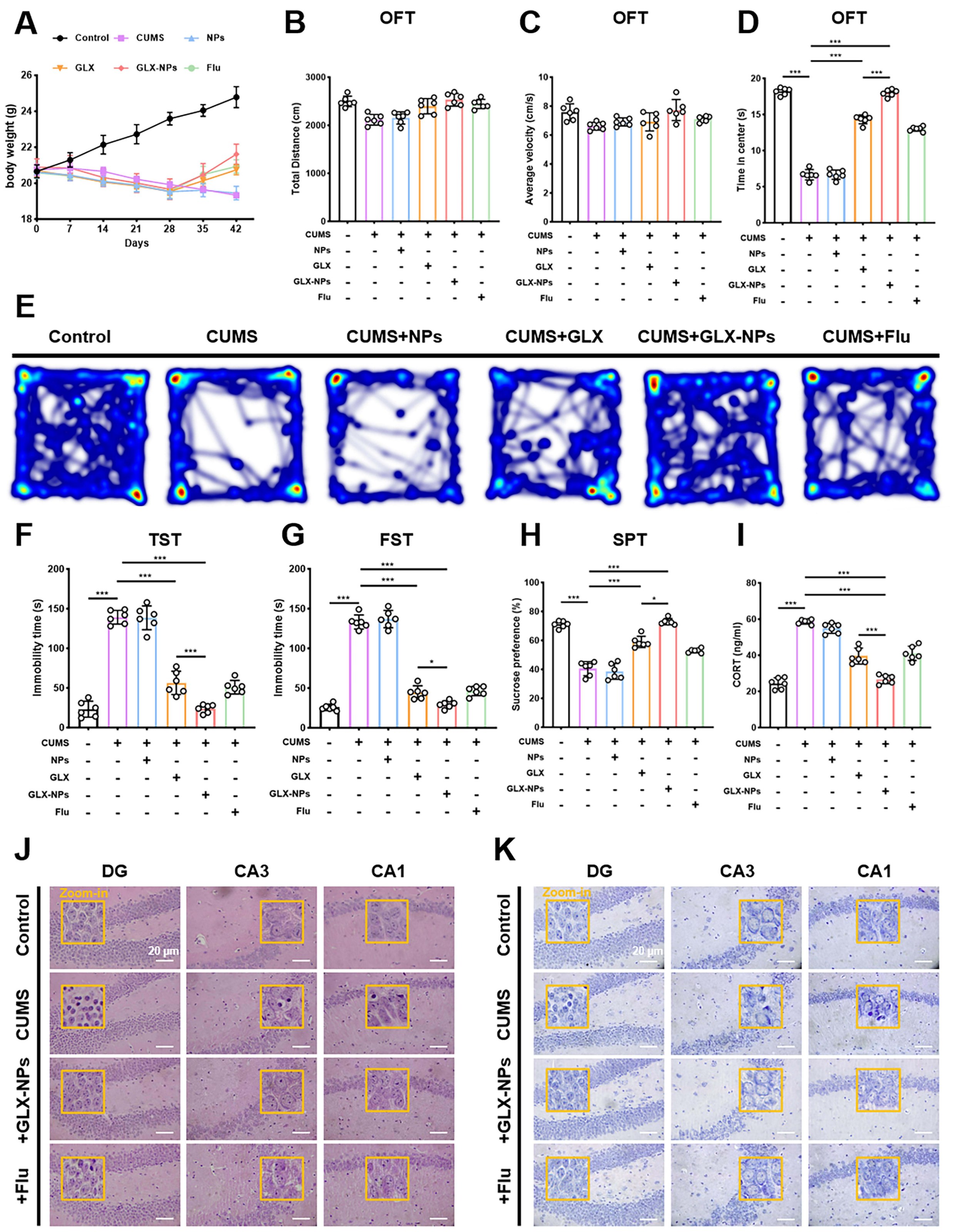

Figure 2 GLX-NPs alleviate depression-like behaviors in CUMS-exposed mice. (**A**) Body weight of mice (n = 6). (**B**) Average velocity in the OFT (n = 6). (**C**) Total distance traveled in the OFT (n = 6). (**D**) Time spent in the center zone during the OFT (n = 6). (**E**) Representative heatmaps of locomotor trajectories in the OFT. (**F**) Immobility time in the TST (n = 6). (**G**) Immobility time in the FST (n = 6). (**H**) Sucrose consumption in the SPT (n = 6). (**I**) Serum CORT levels (n = 6). (**J**) Representative H&E staining of the hippocampal CA1, CA3, and DG regions. The yellow boxes indicate the zoom-in areas. Scale bar = 20 μm. (**K**) Representative Nissl staining of the hippocampal CA1, CA3, and DG regions in each group. The yellow boxes indicate the zoom-in areas. Scale bar=20 μm. Values are presented as the mean ± SD. *p<0.05, ***p<0.001.

In the OFT, no significant differences were observed among groups in total distance traveled or average movement speed (Figure 2B and C, P>0.05), indicating that general locomotor activity remained unaffected. However, CUMS-exposed mice exhibited a significant reduction in time spent in the center zone, suggestive of heightened anxiety or avoidance behavior. Treatment with either free GLX or GLX-NPs markedly increased the time spent in the center, indicating a restoration of exploratory behavior (Figure 2D and E). In both the TST and FST, CUMS model mice displayed significantly prolonged immobility times, a hallmark of depressive-like behavior. Following treatment with GLX or GLX-NPs, immobility times were significantly reduced, reflecting improved affective states. Notably, GLX-NPs were more effective than free GLX in reducing immobility duration, indicating superior antidepressant efficacy (Figure 2F and G). The results of the SPT further corroborated these findings. CUMS exposure significantly reduced sucrose preference, reflecting anhedonia. Both GLX and GLX-NPs reversed this reduction, with GLX-NPs exhibiting a stronger restorative effect, comparable to that of the positive control, Flu (Figure 2H). To validate the effectiveness of the CUMS model and elucidate the biological basis of the antidepressant effect, serum CORT levels were measured. CUMS treatment significantly elevated CORT levels, whereas administration of GLX, GLX-NPs, or Flu markedly attenuated this increase (Figure 2I).

GLX-NPs Treatment Attenuates Neuronal Damage in Mice Exposed to CUMS

To assess the structural impact of CUMS exposure on hippocampal neurons and the potential neuroprotective effects of GLX-NPs, histopathological analyses were performed on the CA1, CA3, and DG regions of the hippocampus using HE and Nissl staining.

HE staining results revealed that hippocampal neurons in the control group were well-organized, with clear cellular contours and intact structures (Figure 2J). Nuclei appeared round or oval with well-defined morphology. In contrast, hippocampal neurons from CUMS-exposed mice exhibited pronounced pathological alterations, including disorganized neuronal arrangement, blurred nuclear boundaries, loss of nucleoli, and a marked increase in the number of necrotic cells—indicating substantial neuronal damage induced by chronic stress. Notably, treatment with GLX-NPs or Flu ameliorated these histological abnormalities, as evidenced by more orderly cell arrangements and reduced numbers of necrotic cells, suggesting partial reversal of CUMS-induced neuronal injury. These findings were further corroborated by Nissl staining (Figure 2K). In the CUMS group, neuronal damage and reduction in Nissl bodies was observed in the CA1, CA3, and DG regions, indicative of impaired neuronal protein synthesis and function. In contrast, GLX-NPs and fluoxetine treatment restored the density and distribution of Nissl bodies in these areas, suggesting an improvement in neuronal integrity and function.

Collectively, these results demonstrate that GLX-NPs effectively alleviate the morphological and functional neuronal damage associated with CUMS exposure, highlighting their potential neuroprotective properties.

The Antidepressant Effect of GLX-NPs Is Reversed by RSL3

To further elucidate whether the antidepressant effects of GLX-NPs are mechanistically associated with the regulation of ferroptosis, we administered the ferroptosis inducer RSL3 and the ferroptosis inhibitor Fer-1 to CUMS-exposed mice and evaluated their behavioral responses through a battery of standardized tests.

In the OFT, mice administered GLX-NPs exhibited a marked increase in central area exploration time. In contrast, co-treatment with RSL3 significantly reduced this exploratory behavior (Figure 3A and B). Similarly, in TST and FST, GLX-NPs significantly reduced immobility time, a key indicator of depressive-like behavior, whereas this effect was notably reduced upon co-treatment with RSL3 (Figure 3C and D). The SPT results further supported these findings, showing that the increased sucrose consumption of GLX-NPs-treated mice was significantly reduced following RSL3 administration (Figure 3E). Additionally, treatment with Fer-1 alone also led to notable improvements in behavioral performance among CUMS mice. Fer-1 administration increased sucrose preference, reduced immobility time in both FST and TST, and prolonged central zone exploration in OFT, demonstrating its intrinsic antidepressant-like potential. Taken together, these results suggest that ferroptosis may play a pivotal role in the pathogenesis of CUMS-induced depressive-like behaviors. The strong reversal of the antidepressant effects of GLX-NPs by RSL3 suggests that GLX-NPs may exert their antidepressant effects by regulating ferroptosis.

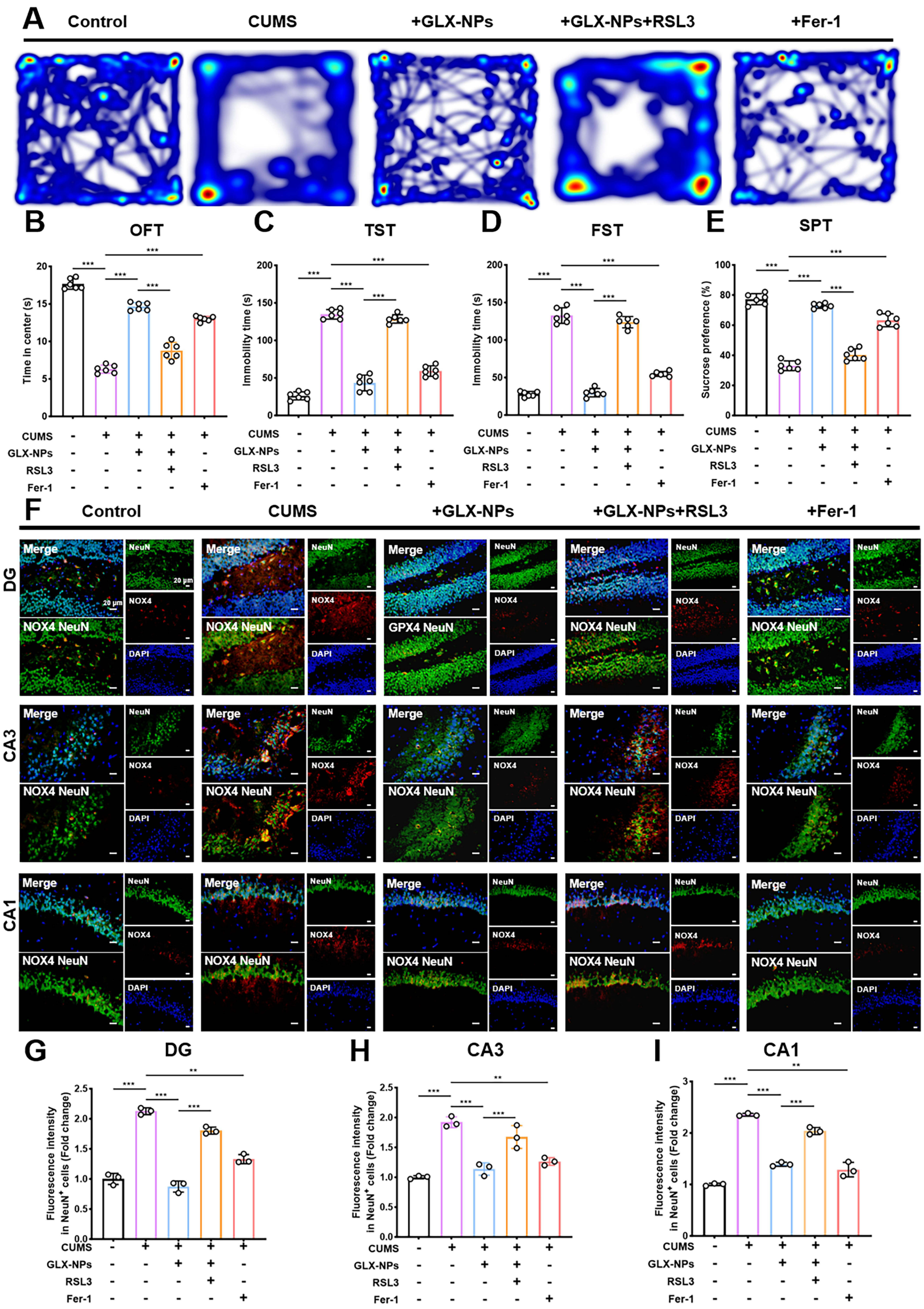

Figure 3 The antidepressant effect of GLX-NPs in CUMS mice is reversed by RSL3. (**A**) Representative heatmaps of locomotor trajectories in the OFT. (**B**) Time spent in the center zone during the OFT (n=6). (**C**) Immobility time in the TST (n=6). (**D**) Immobility time in the FST (n=6). (**E**) Sucrose consumption in the SPT (n=6). (**F**) Representative images of NOX4 and NeuN immunofluorescence staining in the hippocampal CA1, CA3, and DG regions across different groups. Scale bar = 20 μm. (**G**–**I**) Fluorescence quantification of NOX4+/NeuN+ cells in the hippocampus (n=3). Values are expressed as mean ± SD. $^{**}p<0.01$, $^{***}p<0.001$.

GLX-NPs Ameliorate Ferroptosis-Associated Alterations in CUMS-Exposed Mice

GPX4 is a pivotal regulator and classical biomarker of ferroptosis.[36] To further investigate whether GLX-NPs exert their antidepressant effects via modulation of the ferroptosis pathway, we performed immunofluorescence staining to assess the expression levels of NOX4 and GPX4 in neurons of the hippocampal DG, CA1, and CA3 regions in mice. Compared with the control group, mice exposed to CUMS exhibited markedly increased NOX4 expression (Figure 3F–I) and significantly reduced GPX4 expression (Figure 4A–D) in hippocampal neurons. Treatment with GLX-NPs significantly suppressed NOX4 expression and restored GPX4 levels, suggesting that GLX-NPs may inhibit ferroptosis by down-regulating NOX4 and activating GPX4. Further mechanistic studies revealed that the ferroptosis inducer RSL3 reversed the regulatory effects of GLX-NPs on NOX4 and GPX4, while the ferroptosis inhibitor Fer-1 also partially enhanced GPX4 expression. These findings support the critical role of ferroptosis in the pathological alterations observed in CUMS mice.

Additionally, Fe^{2+} accumulation and LPO are hallmarks of ferroptosis. We measured levels of Fe^{2+} (Figure 4E), LPO (Figure 4F), and key OS markers, including GSH (Figure 4G), MDA (Figure 4H), and SOD (Figure 4I) in hippocampal tissues. Exposure to CUMS significantly increased Fe^{2+}, MDA, and LPO levels, while reducing GSH and SOD levels, indicating OS and impaired antioxidant defense. GLX-NPs and Fer-1 treatments markedly decreased Fe^{2+}, MDA, and LPO levels, while significantly restoring GSH and SOD, thus reestablishing redox balance. These effects were notably reversed by RSL3.

To evaluate ferroptosis-associated organelle damage, we employed TEM to examine the ultrastructure of hippocampal neuronal mitochondria (Figure 4J). In the CUMS group, mitochondria displayed typical ferroptotic features, including rounded morphology, disrupted or diminished cristae, increased membrane density, and the presence of vacuole-like structures. Both GLX-NPs and Fer-1 treatments significantly ameliorated mitochondrial structural damage, restoring an elongated or elliptical shape with well-organized cristae. However, the protective effects were abolished following RSL3 treatment.

Taken together, our findings indicate that GLX-NPs effectively inhibit ferroptosis in the hippocampus of CUMS mice by suppressing NOX4 expression, enhancing GPX4 activity, reducing ipid peroxidation and mitochondrial damage, and decreasing Fe^{2+} accumulation.

GLX-NPs Inhibit CORT-Induced Ferroptosis in HT22

To investigate whether GLX-NPs exert anti-ferroptotic effects in vitro, we established an in vitro model of CORT-induced injury in HT22 and evaluated the protective effects of GLX-NPs. Initially, the half-maximal inhibitory concentration (IC_{50}) of CORT was determined using a CCK-8 cell viability assay (Figure S3A-B). The results indicated that treatment with 200 μM CORT reduced HT22 cell viability to approximately 50%, which was selected as the optimal concentration for subsequent experiments. We next assessed the impact of varying concentrations of GLX-NPs on HT22 cell viability under CORT-induced injury (Figure S3C). Cells were treated with a gradient of GLX-NPs concentrations, and viability was measured via CCK-8 assay. Results demonstrated that concentrations up to 20 μM of GLX-NPs had no significant cytotoxic effect.

To further elucidate the role of GLX-NPs in regulating ferroptosis, we employed the FerroOrange fluorescent probe to detect intracellular Fe^{2+} levels (Figure 5A and D). CORT treatment significantly elevated Fe^{2+} levels in HT22 cells, consistent with enhanced ferroptotic activity. Both GLX-NPs and Fer-1 effectively suppressed CORT-induced Fe^{2+} accumulation, indicating their inhibitory action on ferroptosis. However, co-treatment with the ferroptosis inducer RSL3 substantially reversed the suppressive effects of GLX-NPs on Fe^{2+} levels, providing further evidence for the anti-ferroptotic role of GLX-NPs in this cellular model.

GLX-NPs Alleviate CORT-Induced Lipid Peroxidation and Mitochondrial Dysfunction in HT22

Given the critical role of mitochondrial dysfunction and lipid peroxidation in the process of ferroptosis,[37,38] we further evaluated the effects of GLX-NPs on mitochondrial integrity and oxidative status in CORT-induced HT22.

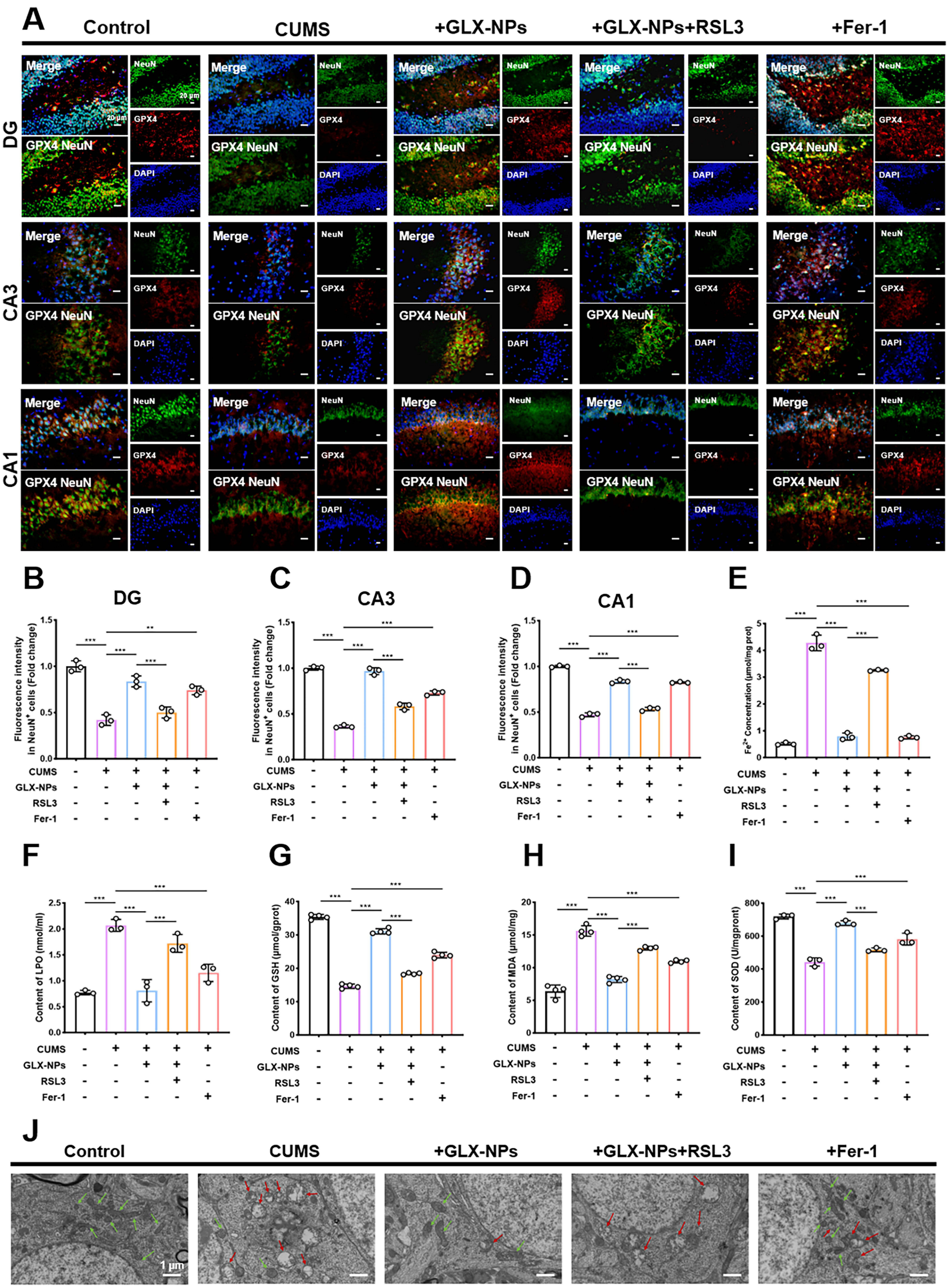

Figure 4 GLX-NPs significantly reduce ferroptosis and OS in CUMS mice. (**A**) Representative immunofluorescence images of GPX4 and NeuN staining in the hippocampal CA1, CA3, and DG regions across different groups. Scale bar = 20 μm. (**B**–**D**) Fluorescence quantification of NOX4+/NeuN+ cells in the hippocampus (n=3). (**E**) Fe^{2+} content in the hippocampus (n = 3). (**F**–**I**) Levels of LPO, MDA, GSH, and SOD in the hippocampus of mice from different groups (n=3-4). (**J**) Representative TEM images of the hippocampus from different treatment groups. Normal mitochondria are indicated by green arrows, and mitochondria with ferroptosis-like features are indicated by red arrows. Scale bar=1 μm. Data are presented as mean ± SD. **p<0.01, ***p<0.001.

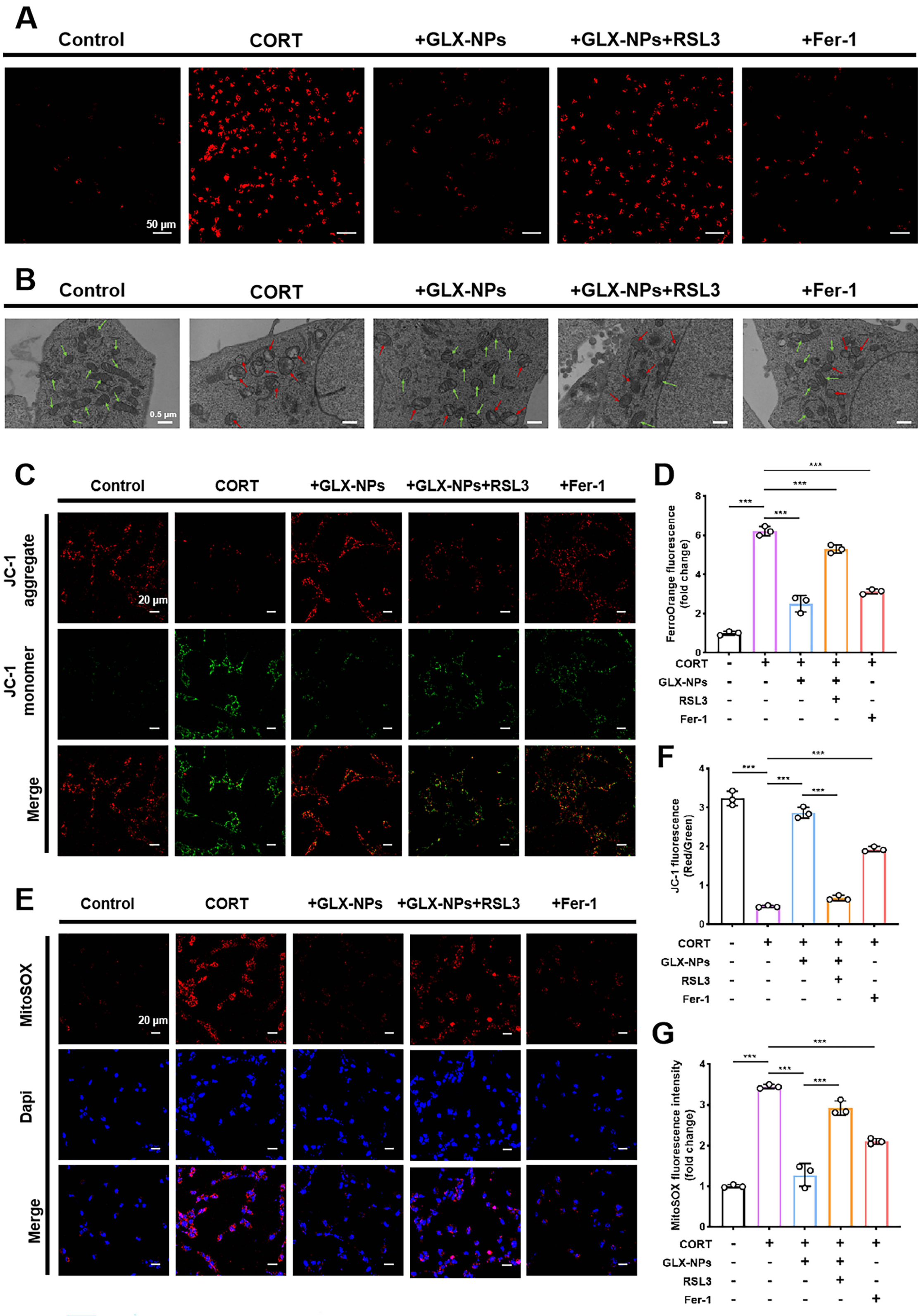

Figure 5 GLX-NPs attenuate CORT-induced ferroptosis, mitochondrial dysfunction, and OS in HT22. (**A** and **D**) Intracellular Fe^{2+} levels detected by FerroOrange and corresponding relative fluorescence intensity (n = 3). Scale bar = 50 µm. (**B**) Representative TEM images showing mitochondrial morphology in HT22 cells from different groups. Normal mitochondria are indicated by green arrows, and mitochondria with ferroptosis-like features are indicated by red arrows. Scale bar = 0.5 µm. (**C** and **F**) Intracellular MMP measured by JC-1 probe, with red and green fluorescence indicating J-aggregates and monomers, respectively (n=3). Scale bar=20 µm. (**E** and **G**) Mitochondrial ROS detected and relative fluorescence intensity measured by MitoSOX probe (n=3). Scale bar = 20 µm. Data are presented as mean ± SD. ***p<0.001.

To assess mitochondrial function, we employed TEM to examine mitochondrial ultrastructure (Figure 5B). Following CORT induction, mitochondria displayed typical pathological features, including swelling, cristae disruption, and disorganized membrane architecture. GLX-NPs treatment significantly ameliorated these structural abnormalities, restoring mitochondrial morphology with intact and well-organized cristae. However, this protective effect was markedly diminished when cells were co-treated with RSL3, further implicating ferroptosis in the observed mitochondrial injury. To further characterize mitochondrial integrity, we used the JC-1 fluorescent probe to measure MMP, a key indicator of mitochondrial activity (Figure 5C and F). Under normal conditions, JC-1 aggregates within mitochondria, emitting red fluorescence, while a reduction in MMP leads to the presence of monomeric JC-1, which emits green fluorescence. CORT exposure significantly decreased MMP in HT22 cells, as evidenced by diminished red fluorescence and increased green fluorescence, indicating pronounced mitochondrial depolarization. Treatment with GLX-NPs or the ferroptosis inhibitor Fer-1 effectively preserved MMP, suggesting robust mitochondrial protective effects. Additionally, CORT exposure markedly increased mitochondrial ROS production (Figure 5E and G), which was substantially attenuated by GLX-NPs and Fer-1, suggesting their potential involvement in activating endogenous mitochondrial antioxidant defenses. These findings collectively indicate that GLX-NPs and Fer-1 can effectively counteract CORT-induced mitochondrial dysfunction in HT22 cells.

Furthermore, we assessed the intracellular lipid peroxidation levels (Figure S4A-B). The results showed that CORT treatment significantly increased the accumulation of intracellular LPO, as evidenced by a marked increase in green fluorescence intensity. In contrast, interventions with GLX-NPs and Fer-1 significantly inhibited the green fluorescence signal, indicating effective suppression of lipid peroxidation.

Measurements of OS biomarkers supported these findings (Figure S4C-E): CORT significantly increased MDA levels and reduced the antioxidant indices GSH and SOD. Conversely, GLX-NPs and Fer-1 significantly decreased MDA levels and restored GSH and SOD expression, demonstrating a rebalancing of redox homeostasis. Furthermore, intracellular ROS levels were quantified via immunofluorescence staining (Figure 6A and B) and flow cytometry (Figure 6C). CORT exposure markedly increased ROS accumulation, whereas GLX-NPs, acting as a NOX4 inhibitor, effectively suppressed ROS generation. Notably, this inhibitory effect was substantially weakened by co-treatment with RSL3, reinforcing the role of ferroptosis in the oxidative damage process.

Taken together, these results demonstrate that GLX-NPs protect HT22 cells from CORT-induced ferroptosis by stabilizing mitochondrial membrane potential, suppressing lipid peroxidation and ROS accumulation, and preserving mitochondrial structure and function. The capacity of GLX-NPs to maintain redox balance may underlie their therapeutic potential in alleviating depression-like behaviors.

GLX-NPs Inhibit Ferroptosis via Modulation of the NOX4/Nrf2/HO-1/GPX4 Pathway Way

To elucidate the molecular mechanisms underlying the anti-ferroptotic effects of GLX-NPs, we investigated the involvement of the NOX4/Nrf2/HO-1/GPX4 signaling axis. WB analysis revealed that GLX-NPs significantly downregulated the expression of NOX4 while upregulating Nrf2 and its downstream antioxidant effectors, HO-1, GPX4, in both in vivo (Figure 6D and E) and in vitro (Figure S5A-E) systems. To confirm whether these changes at the protein level were also reflected transcriptionally, qRT-PCR was performed to assess the mRNA levels of NOX4, Nrf2, HO-1, and GPX4 in hippocampal tissue (Figure S6A-D) and HT22 (Figure S6E-H). The qRT-PCR results were consistent with the WB data, further substantiating the regulatory role of this pathway in the anti-ferroptotic action of GLX-NPs. Immunofluorescence staining provided direct visual evidence of pathway dynamics (Figure 6F). In CORT-treated HT22, NOX4 expression was markedly upregulated, whereas Nrf2, HO-1, and GPX4 levels were significantly reduced. Treatment with GLX-NPs not only decreased NOX4 expression but also promoted nuclear translocation of Nrf2, leading to the activation of its downstream antioxidant cascade, including increased expression of HO-1 and GPX4. These findings collectively confirm that GLX-NPs inhibit ferroptosis by enhancing antioxidant defense via Nrf2 pathway activation.

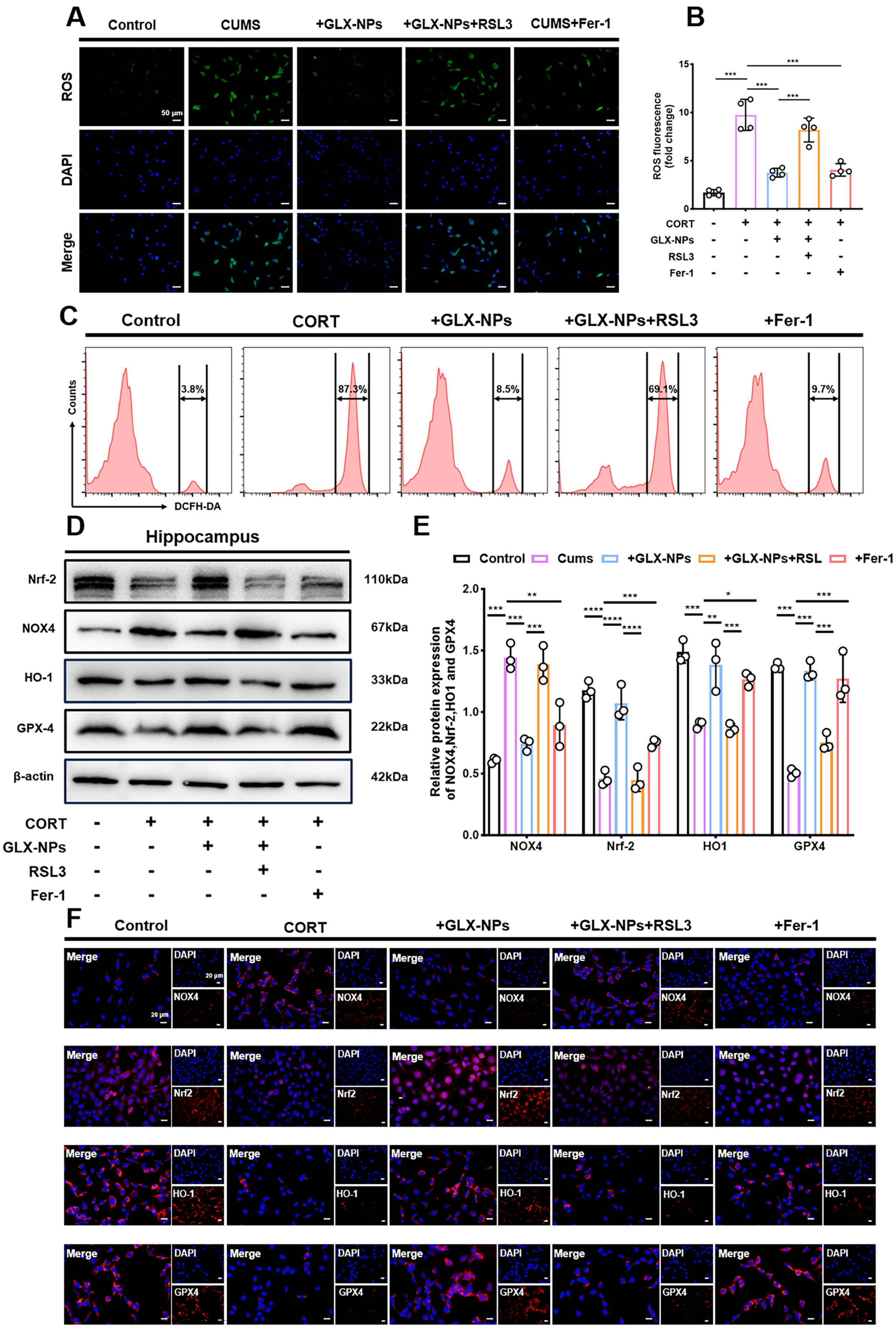

Figure 6 GLX-NPs Attenuate Oxidative Stress and Ferroptosis via Modulating the NOX4/Nrf2/HO-1/GPX4 Pathway. (**A** and **B**) ROS levels detected in HT22 cells and relative fluorescence intensity. Scale bar = 50 μm (n=3). (**C**) Flow cytometry analysis of ROS in HT22 cells from different groups. (**D** and **E**) Representative immunoblotting and quantitative analysis of NOX4, Nrf2, HO-1, and GPX4 of hippocampal tissue from mice in different groups (n=3). (**F**) Representative immunofluorescence images of NOX4, Nrf2, HO-1, and GPX4 in HT22 cells from different groups. Scale bar=20 μm. Data are presented as mean ± SD. *p<0.05, **p<0.01, ***p<0.001, ****p<0.0001.

To further validate the central role of Nrf2 in this regulatory cascade, we administered ML385, a specific Nrf2 inhibitor, and evaluated both behavioral and molecular outcomes. Behavioral analyses showed that ML385 significantly attenuated the antidepressant-like effects of GLX-NPs in CUMS mice, as reflected by decreased exploration in the center zone during the OFT, increased immobility time in both the TST and FST, and reduced sucrose preference (Figure 7A–D).

At the molecular level, both WB (Figure 7E–H, Figure S7A-D) and qRT-PCR (Figure 7I–K, Figure S7E-G) analyses demonstrated that ML385 suppressed the expression of Nrf2, HO-1, and GPX4, and notably inhibited the upregulation of these targets induced by GLX-NPs. Immunofluorescence imaging further confirmed that ML385 effectively blocked the nuclear translocation of Nrf2, thereby impeding the activation of its downstream antioxidant effectors (Figure 7L).

In summary, our findings demonstrate that GLX-NPs mitigate neuronal ferroptotic damage by modulating the NOX4/Nrf2/HO-1/GPX4 signaling axis. These results provide critical mechanistic insight into the neuroprotective and anti-depressant properties of GLX-NPs, highlighting their potential as therapeutic agents for depression-related neuropathology.

Discussion

We successfully encapsulated GLX in mPEG-PCL using the nanoprecipitation method and conducted a detailed characterization of their particle size, ζ potential, morphology, DL, EE, biodistribution and crystallographic changes. The results showed that the GLX-NPs exhibited particle sizes and a mildly negative ζ potential consistent with previous studies,[11,39] with a particle size of less than 60 nm, allowing efficient penetration of the BBB and increased opportunity for drug accumulation in brain tissue. Moreover, positively charged nanoparticles are more readily captured by macrophages in the lungs, liver, and spleen, whereas neutral or negatively charged nanoparticles demonstrate longer circulation times in vivo.[40] Wei et al also confirmed that nanoparticles with a mildly negative ζ potential maintain good stability, with a circulation duration of up to 4 weeks.[10] Crystallographic analysis further revealed changes in the crystalline form of the drug upon encapsulation in nanoparticles. The XRD patterns showed that GLX initially in a crystalline form transformed into an amorphous state after encapsulation in nanoparticles. This transformation is crucial, as amorphous drugs typically exhibit higher solubility and faster absorption rates, which is particularly important for enhancing drug delivery to brain tissue to achieve the desired therapeutic effect. Furthermore, our HPLC measurements indicated that GLX-NPs displayed more stable distribution in brain tissue. At 12 and 24 hours post-administration, the concentration of GLX-NPs in mouse brain tissue was 1.3-fold and 2-fold higher than that of GLX, respectively. In vitro release studies demonstrated that GLX-NPs released the drug more slowly and sustained its release over time, prolonging its action. These results suggest that GLX-NPs possess excellent drug delivery performance, significantly enhancing their translational potential for the treatment of CNS disorders.

To evaluate the therapeutic effects of GLX-NPs in depression, we used the CUMS mouse model as an in vivo experimental model. The results showed that GLX-NPs effectively alleviated depressive-like behaviors in mice, including anhedonia and despair-like behavior, without affecting their spontaneous activity. This finding is consistent with the study by Wang et al, which suggested that changes in spontaneous activity may be related to CNS inhibition.[41] Therefore, our results confirm that GLX-NPs did not impair motor function in mice. Depressive behavioral deficits are often associated with elevated levels of CORT, a steroid hormone that provides the necessary energy to cope with stress and regulates the body's stress response. However, prolonged elevation of CORT levels due to chronic stress has negative effects on the nervous system, leading to emotional and behavioral abnormalities. This result has been confirmed in both this study and previous research.[42] Our research demonstrates that GLX-NPs reduce CORT levels in serum and significantly improve depressive-like behaviors. In addition, Numerous studies have shown that structural and functional impairments of hippocampal neurons are the underlying causes of emotional and cognitive dysfunctions in depression.[43] Wang et al found that hippocampal neurons in CUMS-treated mice exhibited histological abnormalities, including disordered neuronal arrangement and cell death.[44] This finding aligns with our study, and after treatment with GLX-NPs and fluoxetine, the structure and function of hippocampal neurons were partially restored, further confirming the neuroprotective effects of GLX-NPs.

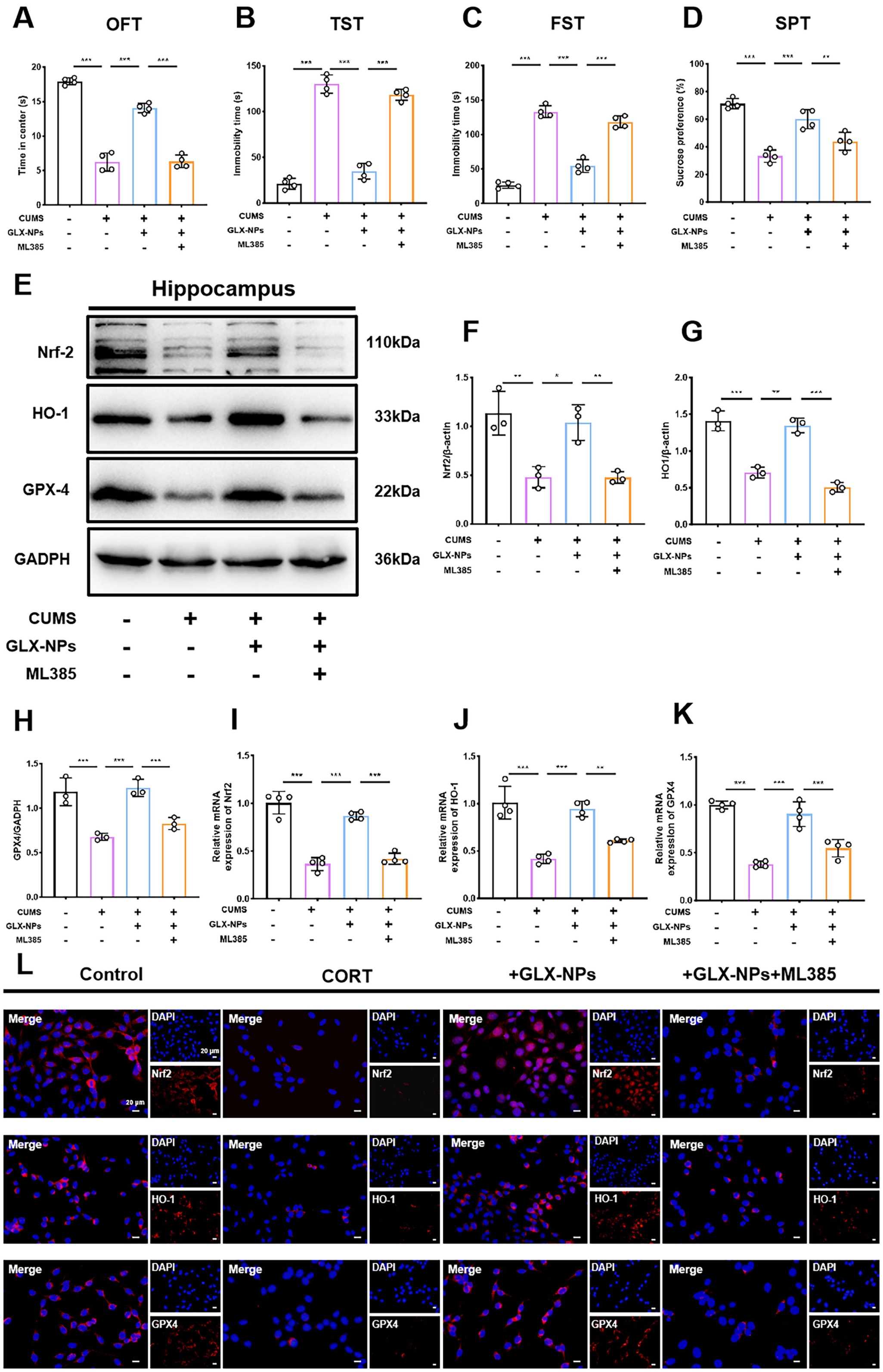

Figure 7 ML385 reverses the antidepressant effects of GLX-NPs. (**A**) Time spent in the center during the OFT (n=6). (**B**) Immobility time in the TST (n=6). (**C**) Immobility time in the FST (n=6). (**D**) Sucrose consumption in the SPT (n=6). (**E**–**H**) Representative immunoblotting and quantitative analysis of Nrf2, HO-1, and GPX4 of hippocampal tissue from mice in different groups (n=6). (**I**–**K**) qPCR analysis of Nrf2, HO-1, and GPX4 expression levels in hippocampal tissue of mice from different groups. (**L**) Representative immunofluorescence images of Nrf2, HO-1, and GPX4 in HT22 cells from different groups (n=3). Scale bar = 20 μm. Data are presented as mean ± SD. *$p<0.05$, **$p<0.01$, ***$p<0.001$.

Numerous studies have demonstrated that NOX4, as a major enzyme responsible for ROS production, plays a crucial role in neurological disorders. It is widely distributed in neuronal cell membranes and various organelles, including mitochondria.[45,46] OS is considered one of the core mechanisms underlying the development of depression,[47] and the role of NOX4 in this process cannot be overlooked. Arab et al found that elevated NOX4 levels were closely associated with depression induced by Chronic Restraint Stress.[42] In this study, we observed a significant increase in NOX4 expression in the hippocampal neurons of CUMS-exposed mice and in CORT-stimulated HT22 cells. GLX-NPs effectively downregulated NOX4 expression, reduced the generation of cellular ROS and mtROS, and protected neurons from OS-induced damage.

One of the consequences of increased ROS production is the induction of ferroptosis, a form of cell death driven by excessive lipid peroxidation.[48] Previous studies have shown that inhibiting NOX4 can suppress ferroptosis in astrocytes and enhance cellular antioxidant defenses, thereby alleviating the progression of neurodegenerative diseases.[49,50] In this study, we observed that hippocampal neurons in CUMS-induced mice and CORT-stimulated neuronal cells exhibited typical characteristics of ferroptosis, including significant lipid peroxidation imbalance, GPX4 depletion, intracellular iron accumulation, and mitochondrial damage. GLX-NPs effectively restored the levels of antioxidant defense factors (GSH, SOD) and reduced the expression of lipid peroxidation markers (LPO, MDA). GPX4, a key regulator of ferroptosis, inhibits lipid peroxidation and maintains membrane integrity. Researchers have found that both gene knockdown of Gpx4 and regulation of GPX4 expression with various inducers have profound effects on ferroptosis-mediated diseases.[51,52] In this study, we verified the reduction of GPX4 levels following depression through multiple approaches. Additionally, the role of Fe^{2+} in ferroptosis cannot be overlooked, as they catalyze the generation of highly reactive hydroxyl radicals via the Fenton reaction, which attack polyunsaturated fatty acids in the cell membrane, initiating lipid peroxidation and accelerating ferroptosis.[37] In our study, the accumulation of Fe^{2+} was closely associated with neuronal damage following depression, further confirming the link between depression and ferroptosis. Notably, mitochondrial dysfunction is one of the potential mechanisms of depression, closely related to abnormalities in neuronal energy metabolism.[53] Therefore, we assessed mitochondrial damage through electron microscopy. Neuronal cells under chronic stress exhibited abnormal mitochondrial morphology, showing hallmark features of ferroptosis,[23,46] including mitochondrial swelling, cristae structure disruption, and increased membrane density. We observed that GLX-NPs treatment significantly improved these pathological changes, enhanced cellular antioxidant capacity, restored GPX4 levels, reduced Fe^{2+} accumulation, and improved mitochondrial morphology. Importantly, the ferroptosis activator RSL3 reversed the behavioral and molecular effects of GLX-NPs, further indicating that the inhibition of ferroptosis plays a central role in the antidepressant effects of GLX-NPs.

Nrf2 is a key transcription factor in maintaining cellular redox homeostasis and plays a critical role in OS,[54] working in conjunction with its downstream target genes HO-1 and GPX4 to form the classic antioxidant and ferroptosis-related signaling pathway.[55] Several natural antioxidant compounds have been found to alleviate the progression of neurodegenerative diseases by modulating the NOX4/Nrf2/GPX4 pathway. In this study, we observed that GLX-NPs downregulated the expression of NOX4 while promoting Nrf2 activation and nuclear translocation, leading to the upregulation of HO-1 and GPX4 expression. This finding supports the mechanism by which GLX-NPs alleviate OS and mitigate ferroptosis through NOX4 inhibition. Conversely, treatment with the Nrf2 inhibitor ML385 significantly reversed the antidepressant effects of GLX-NPs, as evidenced by reduced Nrf2 expression, impaired nuclear translocation, and decreased levels of HO-1 and GPX4. These results indicate that Nrf2 plays a key role in the ferroptosis inhibition mediated by GLX-NPs, further supporting that GLX-NPs effectively suppress neuronal ferroptosis through the NOX4/Nrf2/HO-1/GPX4 signaling pathway, thereby mitigating the pathological damage of depression. This discovery not only provides a new strategy for the treatment of depression but also offers new targets for the study of the underlying mechanisms of depression. Future research can further explore the application of nanotechnology in the treatment of depression, especially its potential in regulating ferroptosis, to provide more effective interventions for precision treatment of depression.

Conclusion

We successfully encapsulated GLX in mPEG-PCL nanomicelles and demonstrated its ability to penetrate brain tissue. Our study reveals that GLX-NPs exert neuroprotective effects by mitigating ferroptosis through the NOX4/Nrf2/HO-1/GPX4 pathway, restoring redox balance, and preserving mitochondrial integrity. These results offer novel insights into the pathophysiology of depression and propose promising therapeutic strategies and potential molecular targets for its treatment.

Ethics Approval and Consent to Participate

This study was approved by the Ethics Review Committee of Jilin University (Approval No. SY. 2024-10-005) and conducted in strict accordance with its guidelines.

Acknowledgments

The authors acknowledge BioRender.com for providing the illustration platform used to create some of the graphical abstract in this work.

Author Contributions

All authors made a significant contribution to the work reported, whether in the conception, study design, execution, acquisition of data, analysis, and interpretation, or in all these areas, took part in drafting, revising, or critically reviewing the article; gave final approval of the version to be published; have agreed on the journal to which the article has been submitted; and agree to be accountable for all aspects of the work.

Funding

This work was funded by National Natural Science Foundation of China (grant number: 81971276), and Science and Technology Development Plan Project of Jilin Province, China (grant number: YDZJ202401402ZYTS, 20240402012GH).

Disclosure

The authors report no conflicts of interest in this work.

References

1. Park LT, Zarate CA. Depression in the primary care setting. *N Engl J Med*. 2019;380:559–568. doi:10.1056/NEJMcp1712493
2. Papakostas GI, Jackson WC, Rafeyan R, Trivedi MH. Inadequate response to antidepressant treatment in major depressive disorder. *J Clin Psychiatry*. 2020;81. doi:10.4088/JCP.OT19037COM5
3. Fournier JC, DeRubeis RJ, Hollon SD, et al. Antidepressant drug effects and depression severity. *JAMA*. 2010;303:47. doi:10.1001/jama.2009.1943
4. Campos AI, Mulcahy A, Thorp JG, et al. Understanding genetic risk factors for common side effects of antidepressant medications. *Commun Med*. 2021;1:45. doi:10.1038/s43856-021-00046-8
5. Himmerich H, Minkwitz J, Kirkby K. Weight gain and metabolic changes during treatment with antipsychotics and antidepressants. *Endocrine Metabolic Immune Disorders-Drug Targets*. 2015;15:252–260. doi:10.2174/1871530315666150623092031
6. Mitter P, De Crescenzo F, Loo Yong Kee K, et al. Sleep deprivation as a treatment for major depressive episodes: a systematic review and meta-analysis. *Sleep Med Rev*. 2022;64:101647. doi:10.1016/j.smrv.2022.101647
7. Licinio J, Wong M-L. Depression, antidepressants and suicidality: a critical appraisal. *Nat Rev Drug Discov*. 2005;4:165–171. doi:10.1038/nrd1634
8. Cheng L, Deng B, Luo W, et al. pH-responsive lignin-based nanomicelles for oral drug delivery. *J Agric Food Chem*. 2020;68:5249–5258. doi:10.1021/acs.jafc.9b08171
9. Torchilin VP. Structure and design of polymeric surfactant-based drug delivery systems. *J Control Release*. 2001;73:137–172. doi:10.1016/S0168-3659(01)00299-1
10. Wei W, Li S, Xu H, et al. MPEG-PCL copolymeric micelles for encapsulation of azithromycin. *AAPS Pharm Sci Tech*. 2018;19:2041–2047. doi:10.1208/s12249-018-1009-0
11. Li G, Shang C, Li Q, et al. Combined Shikonin-loaded MPEG-PCL micelles inhibits effective transition of endothelial-to-mesenchymal cells. *Int J Nanomed*. 2022;17:4497–4508. doi:10.2147/IJN.S374895
12. Meng Q, Meng H, Pan Y, et al. Influence of nanoparticle size on blood–brain barrier penetration and the accumulation of anti-seizure medicines in the brain. *J Mater Chem B*. 2022;10:271–281. doi:10.1039/D1TB02015C
13. Tao W, Yu L, Shu S, et al. miR-204-3p/Nox4 mediates memory deficits in a mouse model of Alzheimer's Disease. *Mol Ther*. 2021;29:396–408. doi:10.1016/j.ymthe.2020.09.006

14. Lin Z, Ying C, Si X, et al. NOX4 exacerbates Parkinson's disease pathology by promoting neuronal ferroptosis and neuroinflammation. *Neural Regen Res*. 2025;20:2038–2052. doi:10.4103/NRR.NRR-D-23-01265
15. Zhao Z, Wang R, Ge H, et al. ECHS1-NOX4 interaction suppresses rotenone-induced dopaminergic neurotoxicity through inhibition of mitochondrial ROS production. *Free Radic Biol Med*. 2025;232:56–71. doi:10.1016/j.freeradbiomed.2025.02.048
16. Bedard K, Krause K-H. The NOX Family of ROS-generating NADPH oxidases: physiology and pathophysiology. *Physiol Rev*. 2007;87:245–313. doi:10.1152/physrev.00044.2005
17. Boonpraman N, Yoon S, Kim CY, Moon J-S, Yi SS. NOX4 as a critical effector mediating neuroinflammatory cytokines, myeloperoxidase and osteopontin, specifically in astrocytes in the hippocampus in Parkinson's disease. *Redox Biol*. 2023;62:102698. doi:10.1016/j.redox.2023.102698
18. Guan L, Mao Z, Yang S, et al. Dioscin alleviates Alzheimer's disease through regulating RAGE/NOX4 mediated oxidative stress and inflammation. *Biomed Pharmacother*. 2022;152:113248. doi:10.1016/j.biopha.2022.113248
19. Miozzo F, Murru L, Maiellano G, et al. Disruption of the autism-associated *Pcdh9* gene leads to transcriptional alterations, synapse overgrowth, and defective network activity in the CA1. *J Neurosci*. 2024:44:e0491242024. doi:10.1523/JNEUROSCI.0491-24.2024
20. Alim I, Caulfield JT, Chen Y, et al. Selenium drives a transcriptional adaptive program to block ferroptosis and treat stroke. *Cell*. 2019;177:1262–1279.e25. doi:10.1016/j.cell.2019.03.032
21. Zha X, Liu X, Wei M, et al. Microbiota-derived lysophosphatidylcholine alleviates Alzheimer's disease pathology via suppressing ferroptosis. *Cell Metab*. 2025;37:169–186.e9. doi:10.1016/j.cmet.2024.10.006
22. Mahoney-Sánchez L, Bouchaoui H, Ayton S, Devos D, Duce JA, Devedjian J-C. Ferroptosis and its potential role in the physiopathology of Parkinson's Disease. *Prog Neurobiol*. 2021;196:101890. doi:10.1016/j.pneurobio.2020.101890
23. Liu J, Kang R, Tang D. Signaling pathways and defense mechanisms of ferroptosis. *FEBS J*. 2022;289:7038–7050. doi:10.1111/febs.16059
24. Yang R, Gao W, Wang Z, et al. Polyphyllin I induced ferroptosis to suppress the progression of hepatocellular carcinoma through activation of the mitochondrial dysfunction via Nrf2/HO-1/GPX4 axis. *Phytomedicine*. 2024;122:155135. doi:10.1016/j.phymed.2023.155135
25. Lv Q, Tao K, Yao X, et al. Melatonin MT1 receptors regulate the Sirt1/Nrf2/Ho-1/Gpx4 pathway to prevent α-synuclein-induced ferroptosis in Parkinson's disease. *J Pineal Res*. 2024;76. doi:10.1111/jpi.12948
26. Wang W, Yang L, Liu T, et al. Corilagin ameliorates sleep deprivation-induced memory impairments by inhibiting NOX2 and activating Nrf2. *Brain Res Bull*. 2020;160:141–149. doi:10.1016/j.brainresbull.2020.03.010
27. Lane DJR, Metselaar B, Greenough M, Bush AI, Ayton SJ. Ferroptosis and NRF2: an emerging battlefield in the neurodegeneration of Alzheimer's disease. *Essays Biochem*. 2021;65:925–940. doi:10.1042/EBC20210017
28. Venkatraman SS, Jie P, Min F, Freddy BYC, Leong-Huat G. Micelle-like nanoparticles of PLA–PEG–PLA triblock copolymer as chemotherapeutic carrier. *Int J Pharm*. 2005;298:219–232. doi:10.1016/j.ijpharm.2005.03.023
29. Li H, Xiang Y, Zhu Z, et al. Rifaximin-mediated gut microbiota regulation modulates the function of microglia and protects against CUMS-induced depression-like behaviors in adolescent rat. *J Neuroinflammation*. 2021;18:254. doi:10.1186/s12974-021-02303-y
30. Wang X, Zhou J, Jiang T, Xu J. Deciphering the therapeutic potential of SheXiangXinTongNing: interplay between gut microbiota and brain metabolomics in a CUMS mice model, with a focus on tryptophan metabolism. *Phytomedicine*. 2024;129:155584. doi:10.1016/j.phymed.2024.155584
31. Cheng Y, Pardo M, de Armini RS, et al. Stress-induced neuroinflammation is mediated by GSK3-dependent TLR4 signaling that promotes susceptibility to depression-like behavior. *Brain Behav Immun*. 2016;53:207–222. doi:10.1016/j.bbi.2015.12.012
32. Wang M, Li M, Jiang Y, et al. Saponins from *Astragalus membranaceus* (Fisch.) Bge alleviated neuronal ferroptosis in Alzheimer's disease by regulating the NOX4/Nrf2 signaling pathway. *J Agric Food Chem*. 2025;73:7725–7740. doi:10.1021/acs.jafc.4c10497
33. Cui Y, Zhang Z, Zhou X, et al. Microglia and macrophage exhibit attenuated inflammatory response and ferroptosis resistance after RSL3 stimulation via increasing Nrf2 expression. *J Neuroinflammation*. 2021;18:249. doi:10.1186/s12974-021-02231-x
34. Dang R, Wang M, Li X, et al. Edaravone ameliorates depressive and anxiety-like behaviors via Sirt1/Nrf2/HO-1/Gpx4 pathway. *J Neuroinflammation*. 2022;19:41. doi:10.1186/s12974-022-02400-6
35. Gustafson HH, Holt-Casper D, Grainger DW, Ghandehari H. Nanoparticle uptake: the phagocyte problem. *Nano Today*. 2015;10:487–510. doi:10.1016/j.nantod.2015.06.006
36. Liu Y, Wan Y, Jiang Y, Zhang L, Cheng W. GPX4: the hub of lipid oxidation, ferroptosis, disease and treatment. *Biochimica et Biophysica Acta (BBA)*. 2023;1878:188890. doi:10.1016/j.bbcan.2023.188890
37. Dixon SJ, Lemberg KM, Lamprecht MR, et al. Ferroptosis: an iron-dependent form of nonapoptotic cell death. *Cell*. 2012;149:1060–1072. doi:10.1016/j.cell.2012.03.042
38. Li J, Jia Y, Ding Y, Bai J, Cao F, Li F. The crosstalk between ferroptosis and mitochondrial dynamic regulatory networks. *Int J Biol Sci*. 2023;19:2756–2771. doi:10.7150/ijbs.83348
39. Luo D, Wang X, Zhong X, et al. MPEG-PCL nanomicelles platform for synergistic metformin and chrysin delivery to breast cancer in mice. *Anticancer Agents Med Chem*. 2022;22:280–293. doi:10.2174/1871520621666210623092725
40. Blanco E, Shen H, Ferrari M. Principles of nanoparticle design for overcoming biological barriers to drug delivery. *Nat Biotechnol*. 2015;33:941–951. doi:10.1038/nbt.3330
41. Valentim JT, Da silva DMA, Capibaribe VCC, et al. Carvacrol alleviates CUMS-induced depressive-like behaviors and cognitive impairment by reducing oxidative stress and neuroinflammation in mice. *Behav Brain Res*. 2024;472:115135. doi:10.1016/j.bbr.2024.115135
42. Arab HH, Khames A, Mohammad MK, et al. Meloxicam targets COX-2/NOX1/NOX4/Nrf2 axis to ameliorate the depression-like neuropathology induced by chronic restraint stress in rats. *Pharmaceuticals*. 2023;16:848. doi:10.3390/ph16060848
43. Price RB, Duman R. Neuroplasticity in cognitive and psychological mechanisms of depression: an integrative model. *Mol Psychiatry*. 2020;25:530–543. doi:10.1038/s41380-019-0615-x
44. Wang Y, Huang Y, Zhao M, et al. Zuojin pill improves chronic unpredictable stress-induced depression-like behavior and gastrointestinal dysfunction in mice via the theTPH2/5-HT pathway. *Phytomedicine*. 2023;120:155067. doi:10.1016/j.phymed.2023.155067
45. Peng C, Li X, Ao F, et al. Mitochondrial ROS driven by NOX4 upregulation promotes hepatocellular carcinoma cell survival after incomplete radiofrequency ablation by inducing of mitophagy via Nrf2/PINK1. *J Transl Med*. 2023;21:218. doi:10.1186/s12967-023-04067-w
46. Boonpraman N, Yi SS. NADPH oxidase 4 (NOX4) as a biomarker and therapeutic target in neurodegenerative diseases. *Neural Regen Res*. 2024;19:1961–1966. doi:10.4103/1673-5374.390973

47. Zuo C, Cao H, Song Y, et al. Nrf2: an all-rounder in depression. *Redox Biol*. 2022;58:102522. doi:10.1016/j.redox.2022.102522
48. Li J, Cao F, Yin H, et al. Ferroptosis: past, present and future. *Cell Death Dis*. 2020;11:88. doi:10.1038/s41419-020-2298-2
49. Xie J, Lv H, Liu X, et al. Nox4-and Tf/TfR-mediated peroxidation and iron overload exacerbate neuronal ferroptosis after intracerebral hemorrhage: involvement of EAAT3 dysfunction. *Free Radic Biol Med*. 2023;199:67–80. doi:10.1016/j.freeradbiomed.2023.02.015
50. Li Z, Lu Y, Zhen Y, et al. Avicularin inhibits ferroptosis and improves cognitive impairments in Alzheimer's disease by modulating the NOX4/Nrf2 axis. *Phytomedicine*. 2024;135:156209. doi:10.1016/j.phymed.2024.156209
51. Zhang W, Liu Y, Liao Y, Zhu C, Zou Z. GPX4, ferroptosis, and diseases. *Biomed Pharmacother*. 2024;174:116512. doi:10.1016/j.biopha.2024.116512
52. Zhang X, Sui S, Wang L, et al. Inhibition of tumor propellant glutathione peroxidase 4 induces ferroptosis in cancer cells and enhances anticancer effect of cisplatin. *J Cell Physiol*. 2020;235:3425–3437. doi:10.1002/jcp.29232
53. Wang G, Cao L, Li S, et al. Gut microbiota dysbiosis-mediated ceramides elevation contributes to corticosterone-induced depression by impairing mitochondrial function. *NPJ Biofilms Microbiomes*. 2024;10:111. doi:10.1038/s41522-024-00582-w
54. Xiang Y, Song X, Long D. Ferroptosis regulation through Nrf2 and implications for neurodegenerative diseases. *Arch Toxicol*. 2024;98:579–615. doi:10.1007/s00204-023-03660-8
55. Sun M, Chen J, Liu F, et al. Butylphthalide inhibits ferroptosis and ameliorates cerebral Ischaemia–Reperfusion injury in rats by activating the Nrf2/HO-1 signalling pathway. *Neurotherapeutics*. 2024; 21:e00444. doi:10.1016/j.neurot.2024.e00444